Spacing and strength of active continental strike-slip faults

Andrew V. Zuza [a,*], An Yin [a,b], Jessica Lin [a], Ming Sun [c]

[a] *Department of Earth, Planetary, and Space Sciences, University of California, Los Angeles, CA 90095-1567, USA*
[b] *Structural Geology Group, China University of Geosciences (Beijing), Beijing 100083, China*
[c] *School of Earth Sciences and Resources, China University of Geosciences (Beijing), Beijing 100083, China*

A B S T R A C T

Parallel and evenly-spaced active strike-slip faults occur widely in nature across diverse tectonic settings. Despite their common existence, the fundamental question of what controls fault spacing remains unanswered. Here we present a mechanical model for the generation of parallel strike-slip faults that relates fault spacing to the following parameters: (1) brittle-crust thickness, (2) fault strength, (3) crustal strength, and (4) crustal stress state. Scaled analogue experiments using dry sand, dry crushed walnut shells, and viscous putty were employed to test the key assumptions of our quantitative model. The physical models demonstrate that fault spacing (S) is linearly proportional to brittle-layer thickness (h), both in experiments with only brittle materials and in two-layer trials involving dry sand overlying viscous putty. The S/h slope in the two-layer sand–putty experiments may be controlled by the (1) rheological/geometric properties of the viscous layer, (2) effects of distributed basal loading caused by the viscous shear of the putty layer, and/or (3) frictional interaction at the sand–putty interface (i.e., coupling between the viscous and brittle layers). We tentatively suggest that this third effect exerts the strongest control on fault spacing in the analogue experiments. By applying our quantitative model to crustal-scale strike-slip faults using fault spacing and the seismogenic-zone thickness obtained from high-resolution earthquake-location data, we estimate absolute fault friction of active strike-slip faults in Asia and along the San Andreas fault system in California. We show that the average friction coefficient of strike-slip faults in the India–Asia collisional orogen is lower than that of faults in the San Andreas fault system. Weaker faults explain why deformation penetrates >3500 km into Asia from the Himalaya and why the interior of Asia is prone to large ($M > 7.0$) devastating earthquakes along major intra-continental strike-slip faults. Our new approach of estimating absolute fault strength may be useful in future studies of continental deformation and earthquake mechanics.

© 2016 Elsevier B.V. All rights reserved.

1. Introduction

Parallel strike-slip faults occur widely in nature, from a few meters to more than hundreds of km in length and spacing (e.g., Segall and Pollard, 1983; Davy and Cobbold, 1988; Swanson, 1988; Martel and Pollard, 1989; Dickinson, 1996; Yin, 2010). Regularly spaced strike-slip faults are observed along plate transform boundaries (e.g., the San Andreas fault system; Fig. 1a) (e.g., Nur et al., 1986; Dickinson, 1996), across collisional orogens (e.g., the Himalayan–Tibetan orogen; Fig. 1b) (Molnar and Tapponnier, 1975; Taylor and Yin, 2009; Yin, 2010; Zuza and Yin, 2016), in analogue experiments (e.g., Tchalenko, 1970; Freund, 1974; Naylor et al., 1986; Yin and Taylor, 2011), and on icy satellites in the outer solar system (e.g., Yin et al., 2016). Irregularly spaced parallel strike-

slip systems have also been documented, including the seismically active right-slip fault systems across northern China where fault spacing varies from ~100 km to ~500 km (e.g., Yin et al., 2015). The characteristic spacing of strike-slip faults, or lack thereof, inevitably reflects how the faults interact with one another and with the fault-bounded crust. Thus, this readily observed geometric parameter may be used to estimate fault strength and stress state across diverse tectonic settings on Earth and other solar system bodies. Despite being such a common feature in zones of lithospheric deformation, the mechanics of evenly-spaced active continental strike-slip faults has never been satisfactorily explained nor quantified.

In this contribution, we develop a stress-shadow model (e.g., Lachenbruch, 1961; Yin et al., 2016) that relates strike-slip-fault spacing to the brittle-crust thickness of the fault-hosting lithosphere, fault and crustal strength, and the remote regional stress. Our model assumptions are tested and validated with scaled analogue experiments using dry sand, dry crushed walnut shells, and

* Corresponding author. Now at: Nevada Bureau of Mines and Geology, University of Nevada, Reno, Nevada 89557, USA.
E-mail addresses: avz5818@gmail.com, azuza@unr.edu (A.V. Zuza).
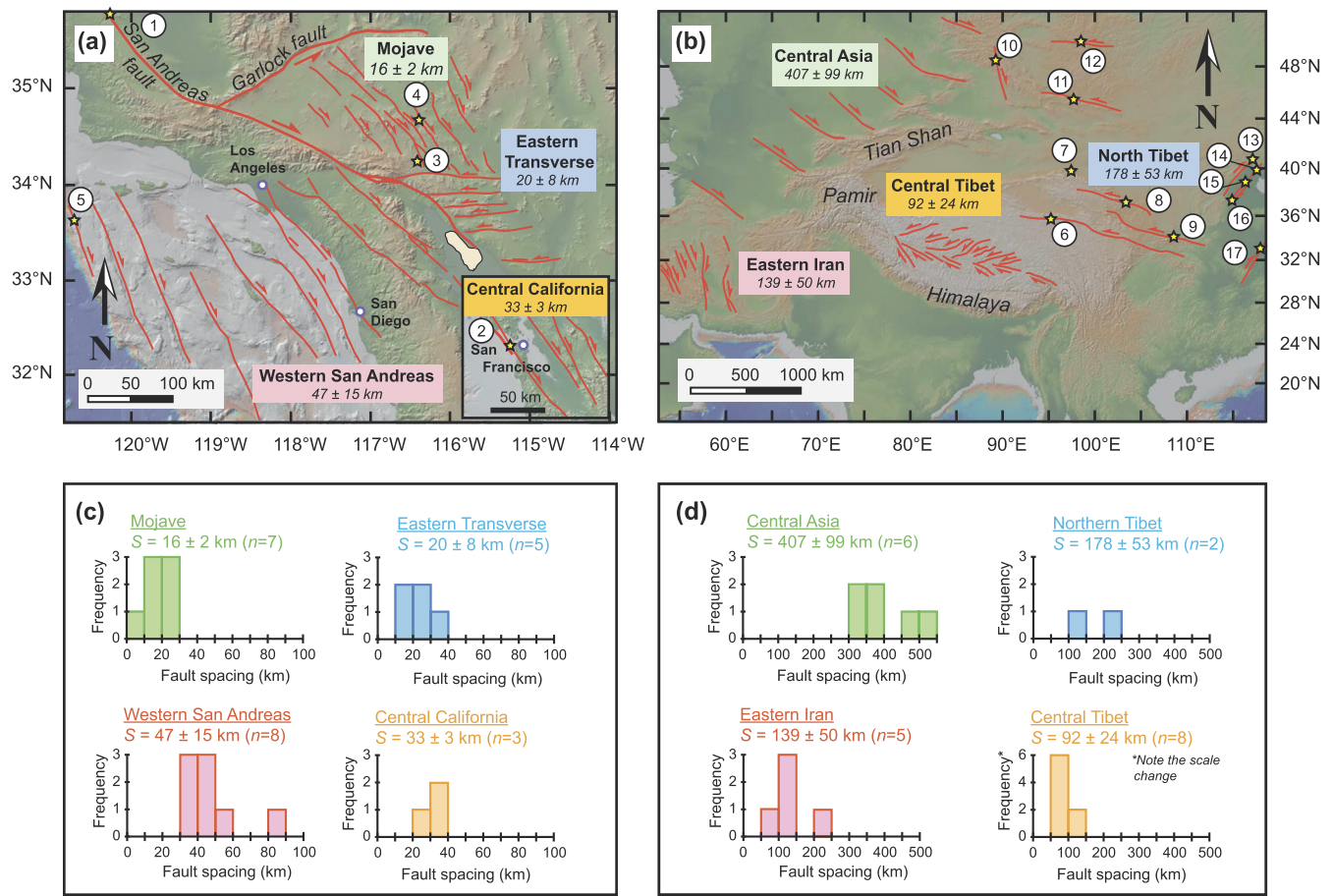
Fig. 1. Evenly-spaced strike-slip fault domains in (a) California and (b) Asia and their average fault spacing. Inset in (a) shows parallel faults in central California. Histograms show fault spacing for each domain of strike-slip faulting in (c) California and (d) Asia. Locations (shown as yellow stars) and magnitudes of major strike-slip fault earthquakes in California and Asia: (1) 1857 M = 7.9 Fort Tejon earthquake, (2) 1906 M = 7.8 San Francisco earthquake, (3) 1992 M = 7.3 Landers earthquake, (4) 1999 M = 7.1 Hector Mine earthquake, (5) 1927 M = 7.3 Lompoc earthquake, (6) 2001 M = 8.1 Kunlun Pass earthquake, (7) 1932 M = 7.6 Changma earthquake, (8) 1920 M = 7.8 Haiyuan earthquake, (9) 1556 M = 8.0 Shaanxi earthquake, (10) 1931 M = 8.0 Fuyun earthquake, (11) 1957 M = 8.1 Gobi Altai earthquake, (12) 1905 M = 8.4 Bulnay earthquake, (13) 1679 M = 8.0 Sanhe-Pinggu earthquake, (14) 1976 M = 7.8 Tanshan earthquake, (15) 1966 M = 7.2 Xingtai earthquake, (16) 1830 M = 7.5 Cixian earthquake, and (17) 1668 M = 8.0 Tancheng earthquake. (For interpretation of the references to color in this figure legend, the reader is referred to the web version of this article.)

viscous putty. These models use a basal shear device to generate Riedel shears in the dry granular materials. By experimenting with various thicknesses and viscosities of a putty layer beneath a brittle layer, we also explore the effects of distributed versus localized basal shear on strike-slip fault spacing.

In this study we show that strike-slip fault spacing is linearly proportional to brittle-layer thickness in both our analogue experiments and for naturally occurring crustal-scale faults. The application of our theoretical model using observed seismogenic zone thickness and fault spacing allows us to estimate the effective coefficient of fault friction ($\overline{\mu_f}$) of strike-slip faults in actively deforming regions on Earth. This method leads to the finding that the faults in the India–Asia collisional orogen are weaker ($\overline{\mu_f} = {\sim}0.10$–$0.20$) than faults in the San Andreas transform system ($\overline{\mu_f} = {\sim}0.15$–$0.22$) in California, which has implications for the mode and extent of continental tectonics away from plate boundaries.

2. Generating parallel strike-slip faults

2.1. Existing models

The following models have been proposed to account for the generation of parallel strike-slip faults: (1) reactivation of preexisting extensional joints in crystalline and/or other low-porosity rock (e.g., Segall and Pollard, 1983; Martel and Pollard, 1989), (2) deformation band formation in high-porosity rocks (e.g., Aydin and Johnson, 1978; Fossen et al., 2007), and (3) viscoelastic models that predict strike-slip fault spacing based on the rheological contrasts of the upper and lower crust (Roy and Royden, 2000a, 2000b).

The first two groups of models explain faulting by a specific sequence of pre- and syn-faulting stress state acting on a particular rock type (e.g., previously normal-faulted rocks or deformation-band generation in porous sandstone) at small spatial scales (i.e., $< {\sim}1$ km). Therefore, they ultimately lack generality for crustal-scale strike-slip faulting in diverse tectonic settings. For example, it is unlikely that strike-slip faulting at a range of scales from <1 mm to >1000s km across diverse lithologies (e.g., Fig. 1) is universally derived from the reactivation of preexisting and regularly-spaced structures. We note that strike-slip faulting in northern Tibet and certain regions of California may be respectively exploiting suture zones and older normal faults (e.g., Taylor and Yin, 2009; Dokka, 1989), but the majority of the faults in both settings actually crosscut preexisting fabrics (Fig. 1) (Dickinson, 1996; Yin and Taylor, 2011). The deformation band mechanism (Aydin and Johnson, 1978) leads to strain localization and strain hardening, which in turn can produce through-going faults. This process predicts sequential initiation and deactivation of individual faults, but does not explain coeval motion of parallel strike-slip faults that occur independent of the fault-hosting lithology.
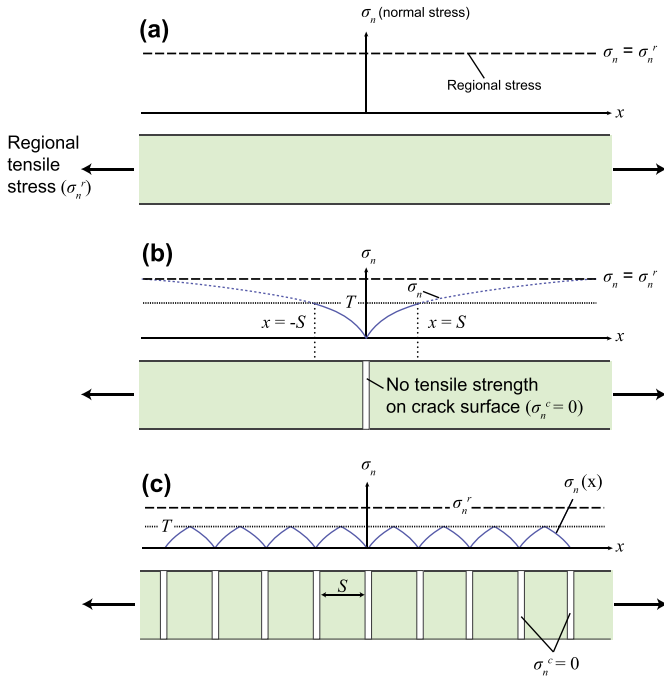
Fig. 2. Conceptual model for the formation of evenly-spaced joints due to the stress shadow effect. (a) A layer under regional extension with a remote normal stress $\sigma_n = \sigma_n^r$. (b) The presence of a fracture causes a local stress reduction and the stress-shadow effect prevents fractures from forming within the strength shadow, with length S. (c) This effect causes fractures in the deforming region to be spaced by this critical distance S. Figure is modified from Yin et al. (2016).

The viscoelastic models of Roy and Royden (2000a, 2000b) examine the effects of rheological stratification on strike-slip faulting. These studies show that fault spacing varies as a function of the strength of the upper crust and viscosity contrast between the upper and lower crust. Two limitations hinder the applicability of these models to actual continent-scale strike-slip faults: (1) the fault-parallel shear stress has an infinite value (i.e., a singularity) at the lower tip of the faults in their dislocation model, and (2) when one fault is active, the other faults are assumed to be completely locked and inactive (i.e., total welding of the other faults), which

implies that the faults are created sequentially, but not active simultaneously as commonly observed on Earth (Fig. 1).

2.2. Stress-shadow model for extensional joints

Our analysis of strike-slip fault spacing employs the stress-shadow concept, which was originally developed to quantify the spacing of extensional joints (Lachenbruch, 1961). Rock under regional remote tensile stress, $\sigma_n = \sigma_n^r$, fails plastically by fracture formation if σ_n^r exceeds the tensile strength of the rock T (Fig. 2). The presence of a new fracture imposes a low stress boundary condition; for extensional joints, the normal stress on the fracture surface σ_n^c is assumed to drop to zero (Pollard and Segall, 1987). This in turns casts a stress shadow within which tensile stress is below the tensile strength of the rock. This condition prohibits fractures from forming adjacent to the initial joint. Stress increases away from the fracture $\sigma_n(x = 0) = \sigma_n^c = 0$ to the regional tensile stress $\sigma_n(x = \infty) = \sigma_n^r$ (Fig. 2). The distance at which σ_n surpasses T defines the stress-shadow length, S, such that $\sigma_n(x = S) = T$ (Fig. 2). New fractures can only be created immediately outside of the stress shadows, resulting in a characteristic joint spacing. The stress rise in the above scenario (Fig. 2) can be quantified by an analytical solution of the stress-distribution for mode-I opening cracks from linear elastic fracture mechanics (LEFM) (Lachenbruch, 1961; Pollard and Segall, 1987; Gross, 1993).

2.3. Stress-shadow model for strike-slip faulting

The stress-shadow model for strike-slip faulting used in this study is based in part on a derivation presented in Yin et al. (2016), which examined strike-slip fault spacing on Enceladus (an icy satellite of Saturn) to infer its ice-shell thickness and frictional strength. In both Yin et al. (2016) and this study, we (1) treat a strike-slip fault as a vertical shear fracture cutting through a brittle layer with its motion driven by a remote fault-parallel shear stress, (2) seek the fault-motion-parallel shear stress distribution, (3) regard the deforming lithosphere as a plastic material governed by the Coulomb fracture criterion, and (4) assume that crustal strength resides dominantly in the brittle crust, consistent with the stress-guide concept (Lister and Davis, 1989) and the current un-
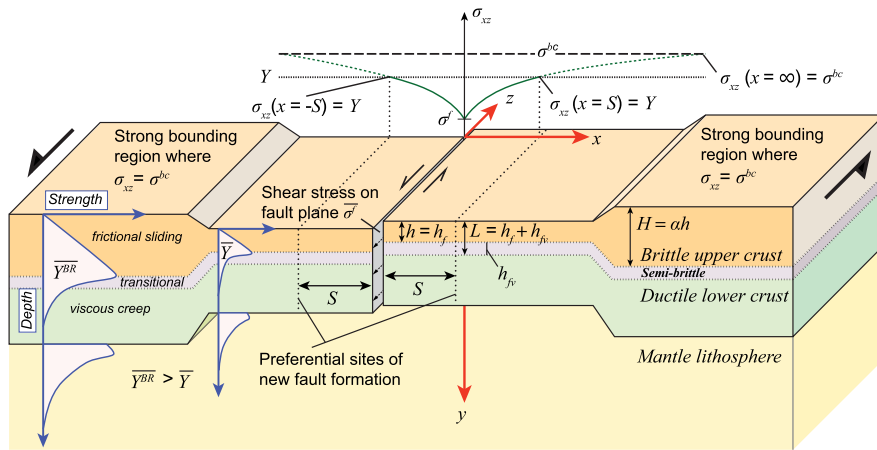
Fig. 3. Model set up, model parameters, and boundary conditions for the formation of evenly-spaced strike-slip faults. Vertically uniform shear stress drives the formation of parallel strike-slip faults in a brittle layer. Off-fault shear stress σ_{xz} satisfies the boundary conditions of $\sigma_{xz}(x = 0) = \sigma^f$ and $\sigma_{xz}(x = \infty) = \sigma^{bc}$. Parameters in the model: σ^f, shear stress on the fault; $\overline{\sigma^f}$, vertically averaged shear strength of the fault; σ^{bc}, regional shear stress in the brittle crust; S, stress-shadow length equal to fault spacing; Y and $\overline{Y}$, shear fracture strength and vertically averaged shear fracture strength of the deforming strike-slip fault domain; $\overline{Y^{BR}}$, vertically averaged shear fracture strength of the stronger bounding region with a thickness H; h, brittle-crust thickness in region of strike-slip faulting; L, seismogenic zone thickness that includes regimes of frictional sliding (h_f) and transitional frictional sliding and viscous creep (h_{fv}); $\alpha = H/h$. Coordinate system and sign convention are shown with red arrows. (For interpretation of the references to color in this figure legend, the reader is referred to the web version of this article.)

derstanding of continental lithosphere rheology (e.g., Jackson et al., 2008).

We first assume that shear stress σ_{xz} satisfies the following boundary conditions (Fig. 3):

$$\sigma_{xz}(x=0) = \overline{\sigma^f} \tag{1a}$$

$$\sigma_{xz}(x=\infty) = \sigma_s^r = \sigma^{bc} \tag{1b}$$

where x is the distance from the fault (Fig. 3), $\overline{\sigma^f}$ is the vertically-averaged shear stress on the fault plane, and σ_s^r is the regional shear stress, which we denote as σ^{bc} ("bc" stands for boundary condition). The boundary condition in equation (1a) is an important departure from the stress-shadow model for extensional jointing, as the magnitude of the shear stress on a strike-slip fault is not zero, but rather equals the vertically averaged shear stress of the fault plane, $\overline{\sigma^f}$ (Fig. 3) (cf. Roy and Royden, 2000a, 2000b). The following solution for the shear stress distribution satisfies the boundary conditions in equations (1a) and (1b):

$$\sigma_{xz}(x) = \sigma^{bc} + \left(\sigma^{bc} - \overline{\sigma^f}\right)\left[\frac{|x|^{n/m}}{(|x|^n + h^n)^{1/m}} - 1\right] \tag{2}$$

where x is the distance from the fault, h is the depth of the fault equal to the brittle-crust thickness in the y direction, $n > 0$, and $m > 0$ (Fig. 3). The above solution is not unique when it is constrained by the boundary conditions alone because it lacks information on the rheology of the deforming fault-hosting material. For example, the following solution also satisfies the boundary conditions shown in equations (1a) and (1b):

$$\sigma_{xz}(x) = \sigma^{bc} + \left(\sigma^{bc} - \overline{\sigma^f}\right)\left[\frac{\tan^{-1}(x)}{\left(\frac{\pi}{2}\right)} - 1\right] \tag{3}$$

where $\tan^{-1}(x=0) = 0$ and $\tan^{-1}(x=\infty) = \frac{\pi}{2}$, thus allowing $\sigma_{xz}(x=0) = \overline{\sigma^f}$ and $\sigma_{xz}(x=\infty) = \sigma^{bc}$. However, as we show below, the solution in equation (2) permits a linear relationship between S and h, which is observed in our analogue experiments and continental strike-slip fault data (see below in sections 3 and 4), whereas equation (3) does not have this mathematical property.

Using equation (2), the length of the stress shadow S can be obtained by:

$$\sigma_{xz}(x=S) = \overline{Y} = \sigma^{bc} + \left(\sigma^{bc} - \overline{\sigma^f}\right)\left[\frac{S^{n/m}}{(S^n + h^n)^{1/m}} - 1\right] \tag{4}$$

where $\overline{Y}$ is the vertically averaged shear fracture strength within the domain of strike-slip faulting (Fig. 3). Note that $\overline{Y}$ is analogous to the tensile strength T in the extensional joint example discussed above.

When $n = m = 2$, equations (2) and (4) have a superficial similarity to the LEFM solution for the shear stress distribution of a mode-III crack embedded in an elastic half space at the Earth's surface (Pollard and Segall, 1987). However, because major continental strike-slip faults cut through the entire brittle crust (e.g., Fig. 1), a "half crack" in an elastic half space is not an ideal approximation (e.g., Yin et al., 2016). The LEFM solution assumes that fracture/fault generation is driven by stress at the free surface, which is viable for cracks in mud, ice, or volcanic rocks (e.g., Lachenbruch, 1961). However, this assumption is inconsistent with fault-parallel stress increasing with depth for continental-scale faulting (see equation [8.44d] in Pollard and Segall, 1987; Gross, 1993), as this would imply that the minimum shear stress at the Earth's surface is primarily responsible for nucleating new faults. Another important difference is that our model does not create a stress singularity at the basal tip of the fault as when

modeled as a half crack in the classic treatment of Pollard and Segall (1987).

A rigorous way of determining the values of m and n is to insert the general solution shown in equation (4) into stress equilibrium equations that are coupled with a rheological model (e.g., elastic, plastic, viscoelastic, etc.) for the deforming material hosting the strike-slip faults. Here we take an empirical approach by observing the relationship between S and h values in nature and controlled laboratory experiments. As shown below, S and h are best described by a linear relationship (i.e., S/h ratios are constant), and this simple observation requires that $m = n = 1$ in equation (4).

3. Analogue modeling

Starting with the observation that extensional-joint spacing is linearly proportional to the thickness of the joint-hosting layer (e.g., Bai and Pollard, 2000), we set out to investigate whether a similar linear relationship holds for strike-slip fault spacing and brittle-layer thickness. Scaled analogue experiments were conducted using dry granular materials, which can simulate brittle-crust deformation (e.g., Davy and Cobbold, 1988). Our experiments use a 12-cm-wide basal-sliding-plate device to generate two parallel shear zones in which Riedel shears form (see Yin and Taylor, 2011) (Fig. 4). The model boundary-wall dimensions (65 cm × 70 cm) are an order of magnitude larger than the width of the shear zones created in the experiments, which are typically ≤6 cm (Fig. 4a).

One set of experiments use a single layer of dry sand or crushed walnut shells to determine the relationship between brittle-layer thickness and fault spacing. The second set of experiments include a ductile putty layer underneath the frictional materials to examine the role of a viscous layer in controlling the relationship between fault spacing and brittle-layer thickness.

3.1. Experimental materials

We use two different granular materials for the brittle layer—commercially available dry sand and crushed walnut shells (e.g., Hubbert, 1937, 1951; Davy and Cobbold, 1988; Cruz et al., 2008)—for two distinct reasons. First, they have different frictional properties, which permits rigorous testing of the predictions made by our analytical model against the results of our analogue experiments. Second, the materials have different densities (i.e., 1670 vs. 790 kg/m^3 for sand and crushed walnut shells, respectively) and thus slightly different scaling relationships between the model and nature (see section 3.2), which again can be used to verify our proposed mathematical model for fault spacing.

The frictional properties of the experimental materials were determined with a Hubbert-type apparatus (Hubbert, 1951), which involves constructing a shear stress versus normal stress failure envelope for each of the experimental materials (e.g., Cruz et al., 2008). The shear stress that generates Riedel shear fractures is a function of the basal friction (μ_b) beneath the sand/crushed walnut shells (see section 4.2). Therefore we quantify μ_b between the (1) granular materials and underlying basal-sliding plate covered by P100 sandpaper (~162 μm grain size) and (2) dry sand and putty layer. This second interface consists of sand embedded in the putty, which creates a sticky sandpaper-like surface. The grain size distributions and measured frictional properties of our granular materials are reported in Table 1 and Fig. A1. All of these procedures were repeated at least five times for each set of experiments to generate statistical uncertainties.

Putty obtained from Isokinetics Inc. was used as the viscous layer underneath the brittle layer. An inclined plane experiment was conducted to determine the approximate viscosity of the putty. The strain rate of simple-shear flow of the putty with an
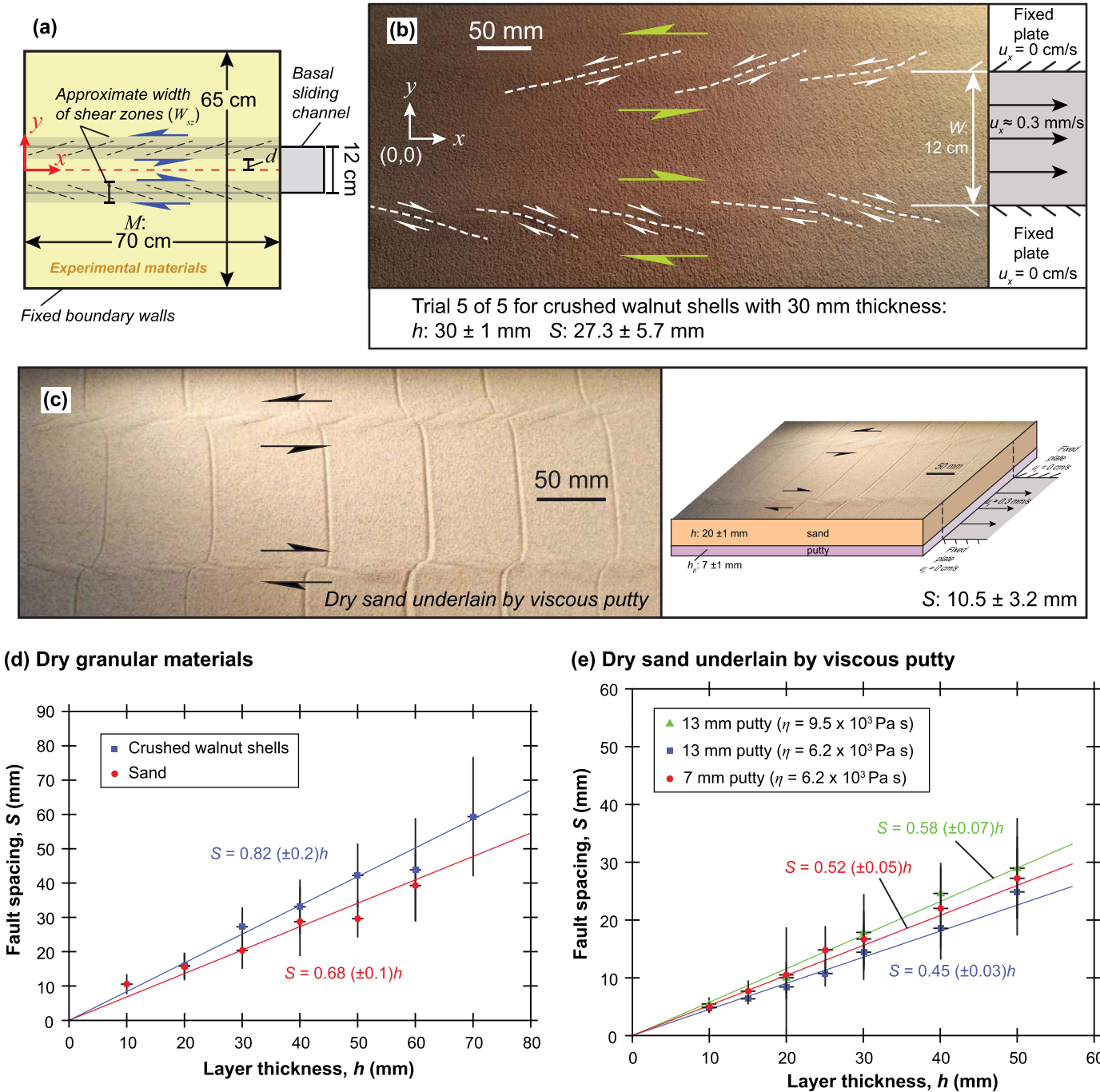
Fig. 4. (a) Plan view of experimental setup with 12-cm-wide basal sliding plate that is used to create to create two parallel shear zones in which Riedel shears form. Note that the resulting shear zone has a length and width of M and W_{sz}, respectively. Also shown is the coordinate axis and d value, which measures the distance from the center of the basal-sliding plate to the Riedel-shear zone. (b) A representative experimental run showing the general apparatus setup and the resulting development of nearly evenly-spaced parallel Riedel shear fractures in two parallel distributed shear zones using crushed walnut shells ($h = 30$ mm). The basal plate moved to the right in this image, which created left- and right-slip shear zones in the top and bottom of the image respectively. (c) Another representative experimental run with 7-mm-thick viscous putty (h_p) overlain by dry sand ($h = 20$ mm). The viscosity of the putty is 6.2×10^3 Pa s. The basal plate in this image moved to the right. (d) Plot of fault spacing versus brittle layer thickness of sand and crushed walnut shells obtained from this study for all experimental runs. The best-fit linear regression is accomplished by forcing the lines through the origin. (e) Plot of fault spacing versus brittle layer thickness of sand underlain by viscous putty of different thicknesses and viscosities. The best-fit linear regression is accomplished by forcing the lines through the origin. (For interpretation of the references to color in this figure legend, the reader is referred to the web version of this article.)

overlying mass on an inclined surface can be used to calculate the viscosity following the relationship $\tau = \eta\dot{\gamma}$, where τ is shear stress, η is viscosity, and $\dot{\gamma}$ is shear strain rate. Note that because of this relationship, our experiments using different viscosity putties also incorporate the effects of variable strain rates. The simple-shear experiments yield viscosities of 6.2×10^3 Pa s and 9.5×10^3 Pa s for the two types of putties.

3.2. Scaling considerations

Relating the analogue experiments to crustal-scale strike-slip faults requires dynamic and geometric scaling governed by the following relationships (Hubbert, 1937):

$$\frac{C^{model}}{C^{nature}} = \frac{\sigma_V^{model}}{\sigma_V^{nature}} = \frac{\rho^{model} \times l^{model} \times g^{model}}{\rho^{nature} \times l^{nature} \times g^{nature}} \tag{5}$$

Table 1
Physical and mechanical properties of experimental materials.

Material	Density (kg/m^3)	Grain size (μm)	$\pm\sigma$	C_0 (Pa)	$\pm\sigma$	μ_φ	$\pm\sigma$	ϕ (°)
Sand	1670	220	86	62.5	10.5	0.50	0.01	26.5
Sand vs sandpaper	–	–	–	51.5	40.5	0.53	0.03	28.1
Sand vs putty/sand	–	–	–	–	–	0.73	0.05	36.1
Crushed walnut shells	790	332	82	36.8	10.2	0.40	0.01	21.6
Walnut shells vs sandpaper	–	–	–	31.0	29.0	0.51	0.04	27.1

μ_φ, coefficient of friction.
ϕ, angle of friction.

where superscripts *model* and *nature* denote the model and crustal parameters and l, σ_V, ρ, and g are vertical thickness, vertical stress, density, and the gravitational acceleration at the Earth's surface, respectively. As the densities of the model and crustal materials are of the same order of magnitude (e.g., 1670 kg/m^3 for sand versus 2750–3100 kg/m^3 for rock), appropriate scaling depends primarily on the model/nature cohesive-strength ratio. The cohesive shear strength of rock varies greatly depending on lithology, ranging from 20 MPa to 110 MPa (Jaeger et al., 2009). Our experimental materials have a cohesive strength (C^{model}) of 40–60 Pa (Table 1), and if we take rock cohesive strength (C^{nature}) to be 50 MPa, we arrive at scaling relationships of sand and crushed walnut shells of $l^{model}_{sand} \approx \sim 1.7 \times 10^{-6} l^{nature}$ and $l^{model}_{walnut} \approx \sim 3.5 \times 10^{-6} l^{nature}$ respectively, where the superscripts *sand* and *walnut* refer to each experimental material. Accordingly, 1 cm sand thickness in our experiments represents ∼6 km crustal thickness. Our experiments, which use layer thicknesses of 1–6 cm for sand and 2–7 cm for crushed walnut shells, can simulate deformation of the crust with overlapping thicknesses of ∼6–35 km and ∼6–21 km for each material, respectively.

3.3. Experimental procedure and results

The first set of experiments was run with dry granular materials (i.e., sand and crushed walnut shells) with thicknesses ranging from 1 cm to 7 cm. Trials run with thicknesses of <1 cm or >7 cm failed to produce observable shear fractures. Sandpaper was used for friction between the materials and the apparatus. In the second series of experiments, the viscous-putty layer was overlain by a sand layer. Both the viscosity and thickness of the putty were varied to observe their effects on fault spacing. Experiments were run with 7-mm- (Fig. 4c) and 13-mm-thick putty layers underneath a dry-sand layer with varying thicknesses (1 to 5 cm). Five trials were repeated for each experiment of varying thicknesses of granular materials. The perpendicular distance between the Riedel shears was measured and the results from all five runs were averaged; the calculated uncertainties are the standard deviation of our observations. Vertical-layer-thickness uncertainty is ∼1 mm.

Results from both sets of experiments can be explained by a simple linear relationships between fault spacing (S) and brittle-layer thickness (h) (Figs. 4d and 4e). For the granular-material-only trials, the following linear relationships are observed: $S/h = 0.68 \pm 0.1$ for sand and $S/h = 0.82 \pm 0.2$ for crushed walnut shells (Fig. 4d).

The experiments with sand overlying a viscous-putty layer all show linear S/h relationships ranging from 0.45 ± 0.03 to 0.58 ± 0.07 (Fig. 4e). A linear regression fits the brittle–viscous experiments within uncertainties, but the range of fault-spacing data for the thicker brittle layers (e.g., when $h > \sim 3–4$ cm) makes a definitive interpretation of this relationships ambiguous (Fig. 4e). For example, the large uncertainties also allow for a nonlinear regressions of this data. However, because a linear relationship is permitted by our observations, we assume the simplest scenario that S and h are linearly proportional. The larger variability of fault

spacing may arise when the fault spacing S and experiment-model length M ratio (S/M) (Fig. 4a) becomes sufficiently high enough that contraction and extension along experimental boundaries affect strike-slip fault generation and spacing.

4. A linear stress-shadow model for strike-slip faulting

4.1. Relationship between fault spacing and brittle-layer thickness

The linear S–h relationship observed in section 3 requires that $n = m = 1$, which allows simplification of equation (4) to the following relationship:

$$S = \frac{\overline{Y} - \overline{\sigma^f}}{\sigma^{bc} - \overline{Y}} h \tag{6}$$

Equation (6) demonstrates that fault spacing S is a function of the (i) brittle-crust thickness h, (ii) regional shear stress acting within the brittle crust σ^{bc}, (iii) shear fracture strength of the deforming brittle crust hosting the active strike-slip faults $\overline{Y}$, and (iv) shear stress on the fault surface $\overline{\sigma^f}$. Fault shear stress and crustal shear strength are pressure-, and therefore, depth-dependent, and their mean values can be obtained by assuming that the normal stresses acting on the existing fault and potential fracture planes are lithostatic. From this assumption, we determine:

$$\overline{\sigma^f} = \frac{1}{h} \int_0^h (C_1 + \overline{\mu_f} \rho g y) \mathrm{d}y = C_1 + \frac{1}{2} \overline{\mu_f} \rho g h \tag{7}$$

and

$$\overline{Y} = \frac{1}{h} \int_0^h (C_0 + \overline{\mu_\varphi} \rho g y) \mathrm{d}y = C_0 + \frac{1}{2} \overline{\mu_\varphi} \rho g h \tag{8}$$

where ρ is the density of the deforming layer, g is the gravitational acceleration, C_0 and $\overline{\mu_\varphi}$ are the cohesive strength and the effective coefficient of internal friction for the crust next to the fault, respectively, and C_1 and $\overline{\mu_f}$ are the cohesive strength of the fault and the effective coefficient of fault friction, respectively. The effective coefficient of internal (i.e., crustal) and fault friction are defined respectively as

$$\overline{\mu_\varphi} = (1 - \lambda_\varphi) \mu_\varphi \tag{9a}$$

$$\overline{\mu_f} = (1 - \lambda_f) \mu_f \tag{9b}$$

where λ_φ and μ_φ are the pore–fluid-pressure ratio and coefficient of internal friction of the fault-bounded domains, respectively, and λ_f and μ_f are the pore–fluid-pressure ratio and coefficient of fault friction, respectively.

To quantify the regional shear stress acting on the boundaries of the strike-slip faulting domains we first assume that shear strength is linearly proportional to the brittle-crust thickness and that the strike-slip domains are bounded by stronger, thus thicker, but still deforming regions (Fig. 3). If strike-slip faulting does not occur
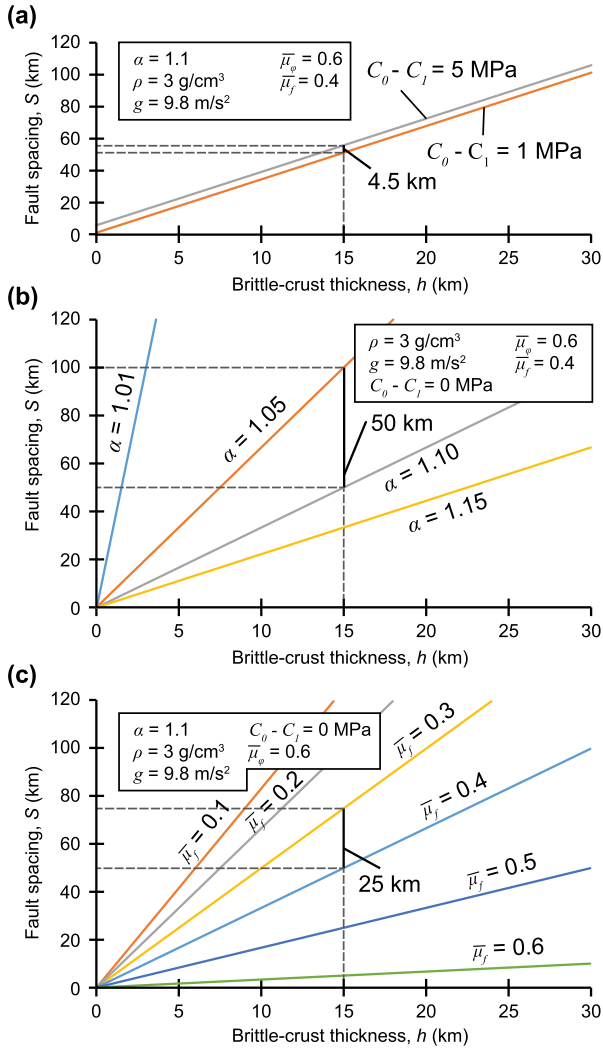
Fig. 5. Effects of model parameters on the relationship between fault spacing and brittle-crust thickness as a function of (a) the difference between fault and crustal cohesive strengths $C_0 - C_1$, (b) α values, and (c) the effective fault friction $\overline{\mu_f}$.

within these adjacent regions, the regional shear stress must be below the shear fracture strength of these stronger and thicker domains. Therefore we assume that the regional stress σ^{bc} equals the vertically averaged shear strength of the stronger but still deforming regions ($\overline{Y^{BR}}$) bounding the strike-slip domain (Fig. 3). That is

$$\sigma^{bc} = \overline{Y^{BR}} = \frac{1}{H} \int_0^H \left(C_2 + \overline{\mu_\varphi^{BR}} \rho g y \right) dy = C_2 + \frac{1}{2} \overline{\mu_\varphi^{BR}} \alpha \rho g h \quad (10)$$

where C_2 and $\overline{\mu_\varphi^{BR}}$ are the cohesive strength and effective coefficient of internal friction of the bounding regions, respectively, H is the brittle-layer thickness of bounding regions, and α is a proxy for regional-stress magnitude defined as $\alpha = H/h > 1$ (Fig. 3). Using $\overline{Y}$, σ^f, and σ^{bc} from equations (7), (8), and (10), and assuming $\overline{\mu_\varphi^{BR}} = \overline{\mu_\varphi}$ and $C_0 = C_2$, we derive the following S–h relationship:

$$S = \frac{(C_0 - C_1) + \frac{1}{2} \rho g h (\overline{\mu_\varphi} - \overline{\mu_f})}{\frac{1}{2} \rho g h \overline{\mu_\varphi} (\alpha - 1)} h \quad (11)$$

Because S is relatively insensitive to $(C_0 - C_1)$ (Fig. 5a), we simplify equation (11) to:

$$S = \frac{(\overline{\mu_\varphi} - \overline{\mu_f})}{\overline{\mu_\varphi}(\alpha - 1)} h \quad (12)$$

and

$$\overline{\mu_f} = \overline{\mu_\varphi} \left[1 - \frac{s}{h}(\alpha - 1) \right] \quad (13)$$

Given that $\overline{\mu_f} > 0$, the following relationship must also hold:

$$\alpha \leq \left(\frac{h}{s} + 1 \right) \quad (14)$$

Equation (14) indicates that for the same brittle-crust thickness, wider fault spacing requires lower values of α. This means that a larger stress magnitude and/or stress gradient (i.e., a larger α value due to stronger bounding crust or weaker deforming crust) leads to more closely spaced strike-slip faulting because the stress rise is more rapid from $\sigma_{xz}(x=0) = \overline{\sigma^f}$ to $\sigma_{xz}(x=S) = \overline{Y}$ (Figs. 3 and 5b). Fault strength $\overline{\mu_f}$ also affects S; larger values of $\overline{\mu_f}$ leads to smaller fault spacing S (Fig. 5c).

4.2. The stress-shadow model and our analogue experiments

The fault-parallel shear stress generated by basal shearing in our analogue experiments differs from the depth-dependent fault-parallel shear stress assumed in our analytical solutions as shown in equation (10). That is, the fault-parallel shear stress in our experiments depends only on the basal coefficient of friction and is independent of the vertical axis when solving the stress equilibrium equations (see derivation in Supplementary Material). Because of this difference, the detailed formation processes of strike-slip faults in nature and in our experiments are slightly different, although the experimental results can be satisfactorily explained by our stress-shadow model as detailed below. First, we obtain an expression for the "sidewall" shear stress ($\sigma_{sidewall}$) on a plane perpendicular to the basal sliding plate and parallel to the sliding direction (see Supplementary Material):

$$\sigma_{sidewall} = \mu_b \rho g y \quad (15)$$

where μ_b is the measured coefficient of friction of the experimental materials against the basal-sliding plate covered in sandpaper (Table 1), and y is the axis parallel to the basal-sliding plate but orthogonal to the sliding direction. We set $y = 0$ at the center of the basal-sliding plate (Figs. 4a and 4b). The relationship in equation (15) states that the sidewall shear stress depends on the coefficient of basal friction and the density of the experimental material; it increases with its distance from the central dividing line of the sliding plate.

Although $\sigma_{sidewall} = \mu_b \rho g y$ goes to infinity as $y \to \infty$, the induced shear stress parallel to the newly created Riedel shears (σ_{fp}) is finite. Evaluation of this value at $y = d$, which marks the edge of the Riedel shear zone (Fig. 4a), involves a transformation of coordinates that leads to the following expression for the effective fault-parallel shear stress (σ_{fp}):

$$\sigma_{fp} = \mu_b \rho g d \cos(2\theta) \quad (16)$$

where d is a distance measured along the y-axis (Fig. 4a) such that $\sigma_{fp}(y = d)$ is greater than the yield strength of the experimental materials and θ is the angle between the basal-shear direction and the Riedel shear orientation ($\sim 16°$ in our experiments) (Figs. 4b and 4c) (Jaeger et al., 2009; Supplementary Material).

5. Continental strike-slip faults

We determine the average spacing of active strike-slip faults in the India–Asia collisional orogen and across the San Andreas transform boundary in California (Fig. 1). Application of the stress-shadow model (i.e., equation (12)) to crustal-scale strike-slip faults

Table 2
Observed fault spacing and seismogenic zone thickness.

	D95 thickness (km)	$\pm\sigma$	D90 thickness (km)	$\pm\sigma$	Fault spacing (km)	$\pm\sigma$
California						
Central California	14.4	1.9	12.8	1.7	33 [ref. 1]	3
Western Southern California	15.7	1.1	14.3	1.2	47 [ref. 2]	15
Mojave	11.9	1.1	10.9	1.3	16 [ref. 3]	2
Eastern Transverse Range	12.1	1.5	11	1.2	20 [ref. 2]	8
Best-fit linear regression of brittle-crust thickness vs. fault spacing for California						
D95: $S = 7.2(\pm1.5)L - 70.0(\pm18.8)$ **D90:** $S = 9.5(\pm1.9)L - 87.5(\pm22.5)$						
Asia						
Central Asia	26.0	4.0	19.0	2.6	407 [ref. 4]	99
Northern Tibet	14.5	0.7	13.5	2.1	178 [ref. 5]	53
Central Tibet	10.7	0.8	9.7	0.6	92 [ref. 6]	24
Iran	13.5	2.1	12.5	2.1	139 [ref. 7]	50
Best-fit linear regression of brittle-crust thickness vs. fault spacing for Asia						
D95: $S = 20.6(\pm6.2)L - 129.5(\pm78.9)$ **D90:** $S = 28.7(\pm8.9)L - 192.6(\pm100.5)$						

Sources: [ref. 1]: Savage and Lisowski (1993); [ref. 2]: Dickinson (1996); [ref. 3]: Dokka and Travis (1990); [ref. 4]: Yin (2010); [ref. 5]: Zuza and Yin (2016); [ref. 6]: Yin and Taylor (2011); [ref. 7]: Bachmanov et al. (2004).

requires knowledge of the brittle-crust thickness (i.e., h in Fig. 3) and coefficient of internal friction ($\overline{\mu_\varphi}$). The latter parameter is well constrained from experimental rock mechanics (e.g., Jaeger et al., 2009). We estimate brittle-crust thickness by identifying the seismogenic zone thickness (L) using high-precision relocated earthquake data from Asia and California.

5.1. Strike-slip faults in California and Asia

Four domains of active parallel strike-slip faults were investigated along the San Andreas system in California (e.g., Dickinson, 1996) and across the India-Asia collision zone (e.g., Yin, 2010) (Fig. 1). Spacing between the faults was measured perpendicular to the fault strike. The average and standard deviation for fault spacing within each domain are given in Table 2.

Strike-slip fault domains are observed on either side of the San Andreas fault (e.g., Dickinson, 1996) (Fig. 1a). In central California near San Francisco, four right-slip faults are parallel to the San Andreas fault (e.g., Savage and Lisowski, 1993), including the Hayward, Calaveras, and Greenville faults from west to east. These faults have an average fault spacing of 33 ± 3 km (Fig. 1c). In southern California west of the San Andreas fault, nine northwest-striking right-slip faults extend from the Western Transverse Range in the north through the borderland region in the south. These faults have an average fault spacing of 47 ± 15 km (Fig. 1c), and the major faults are the Ferrelo, San Clemente–San Isidro, Newport–Inglewood–Rose Canyon, Elsinore, and San Jacinto faults, from west to east (e.g., Dickinson, 1996). East of the San Andreas fault in southern California, the Eastern Transverse Range is comprised of six west-striking left-slip faults: Mammoth Wash–Black Eagle, Salton Creek–Aztec Mines Wash, Chiriaco, Smoke Tree Wash–Victory Pass, Blue Cut, and Pinto Mountain fault zones (e.g., Dickinson, 1996). These faults have an average spacing of 20 ± 8 km (Fig. 1c). Also east of the San Andreas fault but north of the left-slip Pinto Mountain fault, there are eight north-striking right-slip faults in the Mojave domain (Fig. 1a) with an average spacing of 16 ± 2 km (Fig. 1c). They are, from west to east, the Helendale, Lockhard–Lenwood, Gravel Hills–Camp Rock, Blackwater–Calico, Pisgah–Bullion, Ludlow, Bristol Mountain, and Granite Mountain faults (Dokka and Travis, 1990).

Active intra-continental deformation in Asia is the combined result of continental collision in the south and oceanic subduction in the east (e.g., Yin, 2010). A series of active right-slip faults occur in central Asia (e.g., Yin, 2010) (Fig. 1b). These faults, dispersed from the Caspian Sea in the southwest to the southern edge of Lake Baikal in the northeast, have an average fault spacing of 407 ± 99 km (Fig. 1d). Three active east-striking left-slip faults, with an average fault spacing of 178 ± 53 km (Fig. 1d), are present across the northern Tibetan Plateau (Fig. 1b): the Kunlun, Qinling, and Haiyuan faults (e.g., Taylor and Yin, 2009; Zuza and Yin, 2016). The V-shaped conjugate strike-slip faults of central Tibet (Taylor and Yin, 2009; Yin and Taylor, 2011) consist of left-slip faults in the north that merge with right-slip faults to the south (Fig. 1b). The average spacing of these conjugate faults is 92 ± 24 km (Fig. 1d). In Iran, parallel and active north-northwest-striking right-slip faults (Bachmanov et al., 2004) (Fig. 1b) have an average spacing of 139 ± 50 km (Fig. 1d).
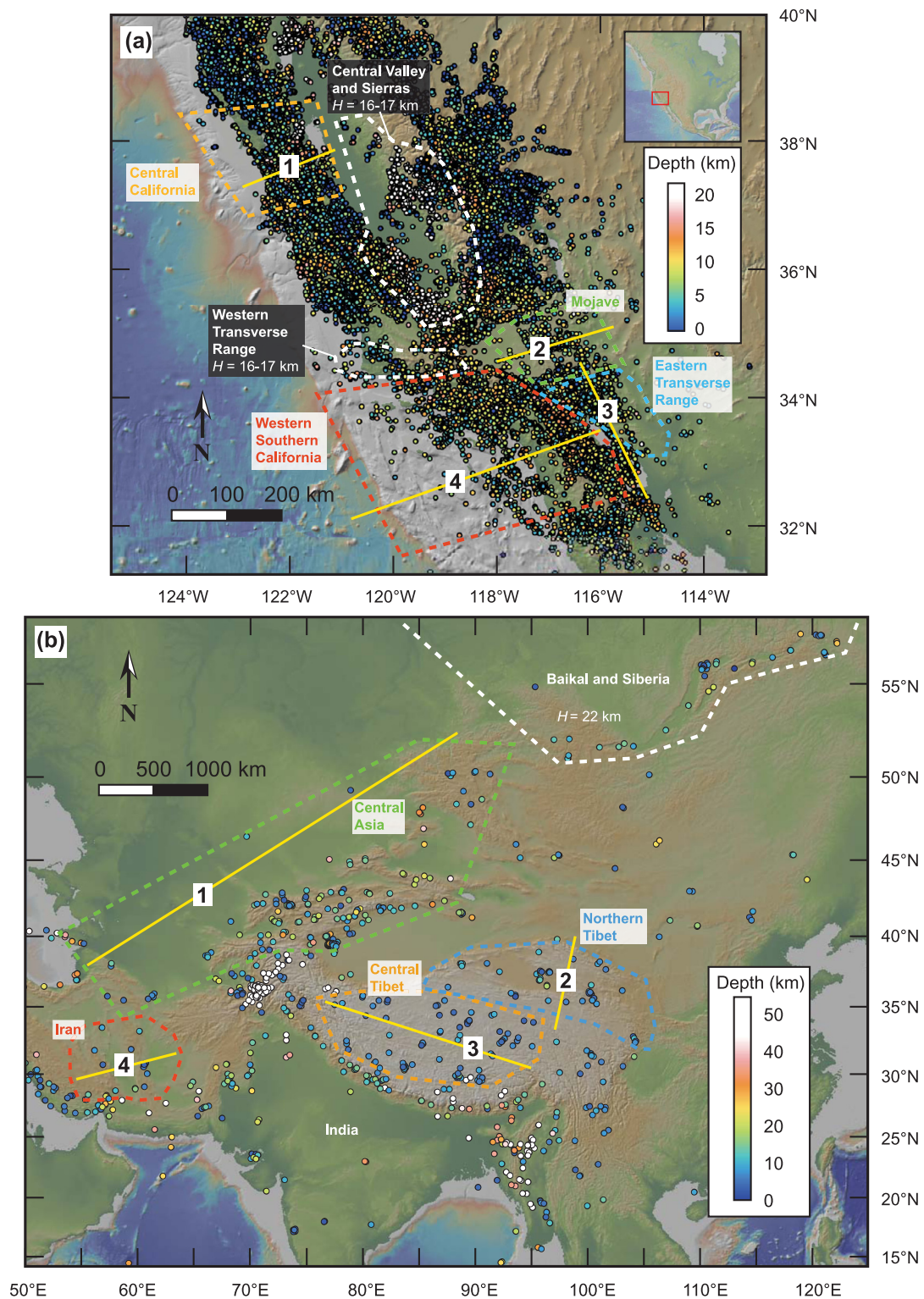
5.2. Seismogenic zone thickness observations

Relocated earthquake location data were compiled for California (Schaff and Waldhauser, 2005; Lin et al., 2007; Waldhauser and Schaff, 2008; Hauksson et al., 2012), Central Asia (Chu et al., 2009; Sloan et al., 2011), Tibet (Chu et al., 2009; Sloan et al., 2011), and Iran (Chu et al., 2009; Sloan et al., 2011; Maggi et al., 2000). Earthquake location data from central California encompasses events from 1984 to 2011 that were relocated by waveform cross correlation and double-difference methods (Schaff and Waldhauser, 2005; Waldhauser and Schaff, 2008). Reported vertical depth errors are less than 0.7 km at 95% confidence. Earthquakes events from 1981 to 2011 are compiled in the southern California earthquake database of Lin et al. (2007) and Hauksson et al. (2012). The relative and absolute vertical depth errors are reported to be less 0.1 km and 1.25 km, respectively, at 90% confidence. In Asia, tele-seismically relocated earthquake-location data span events from 1977 to 1998 (Maggi et al., 2000), 1990 to 2005 (Chu et al., 2009), and 1965 to 2009 (Sloan et al., 2011). Reported vertical errors are <1 km (Chu et al., 2009) and <4 km (Maggi et al., 2000; Sloan et al., 2011).

The compiled earthquake events and their focal depths are plotted in Fig. 6. We seek to determine the depth to the base of the seismogenic zone, and ultimately the brittle-crust thickness from each strike-slip fault domain (Fig. 1). Seismic events from the stronger bounding regions, where strike-slip faulting is not observed, were also examined (Fig. 6) to constrain α. We avoid earthquakes at mantle depths whose occurrences may have been associated with continental subduction, especially near the Pamirs and Tian Shan (Burtman and Molnar, 1993).

Events from each domain were projected onto a vertical plane perpendicular to the strike-slip faults (Fig. 6). Plots of earthquake depth versus horizontal distance along this perpendicu-

Fig. 6. Earthquake-location data from (a) California and (b) Asia. Domains of evenly-spaced strike-slip faults with characteristic fault spacing are outlined. Calculation of seismogenic zone thickness used the data outlined for each domain. The profile numbers correspond to those shown in Fig. A3. Data from Maggi et al. (2000), Schaff and Waldhauser (2005), Lin et al. (2007), Waldhauser and Schaff (2008), Chu et al. (2009), Sloan et al. (2011), and Hauksson et al. (2012).

lar plane are shown in Fig. A3, where the cutoff depth above which 95% (D95) and 90% (D90) seismicity was calculated (Table 2). This was done in several segments along each profile and their average value defines the seismogenic zone thickness (Fig. A3). Specifically, we use segment length of 25 km for Californian faults and 500 to 1000 km for Asian faults (Fig. A3).

The longer segment length for Asian domains reflects the sparse seismic data. Our results show that average fault spacing in California and Asia (Fig. 1) is linearly proportional to the seismogenic zone thickness (Fig. 7a) (Table 2), with a steeper slope for the data from Asia and negative vertical-axis intercepts for both datasets.
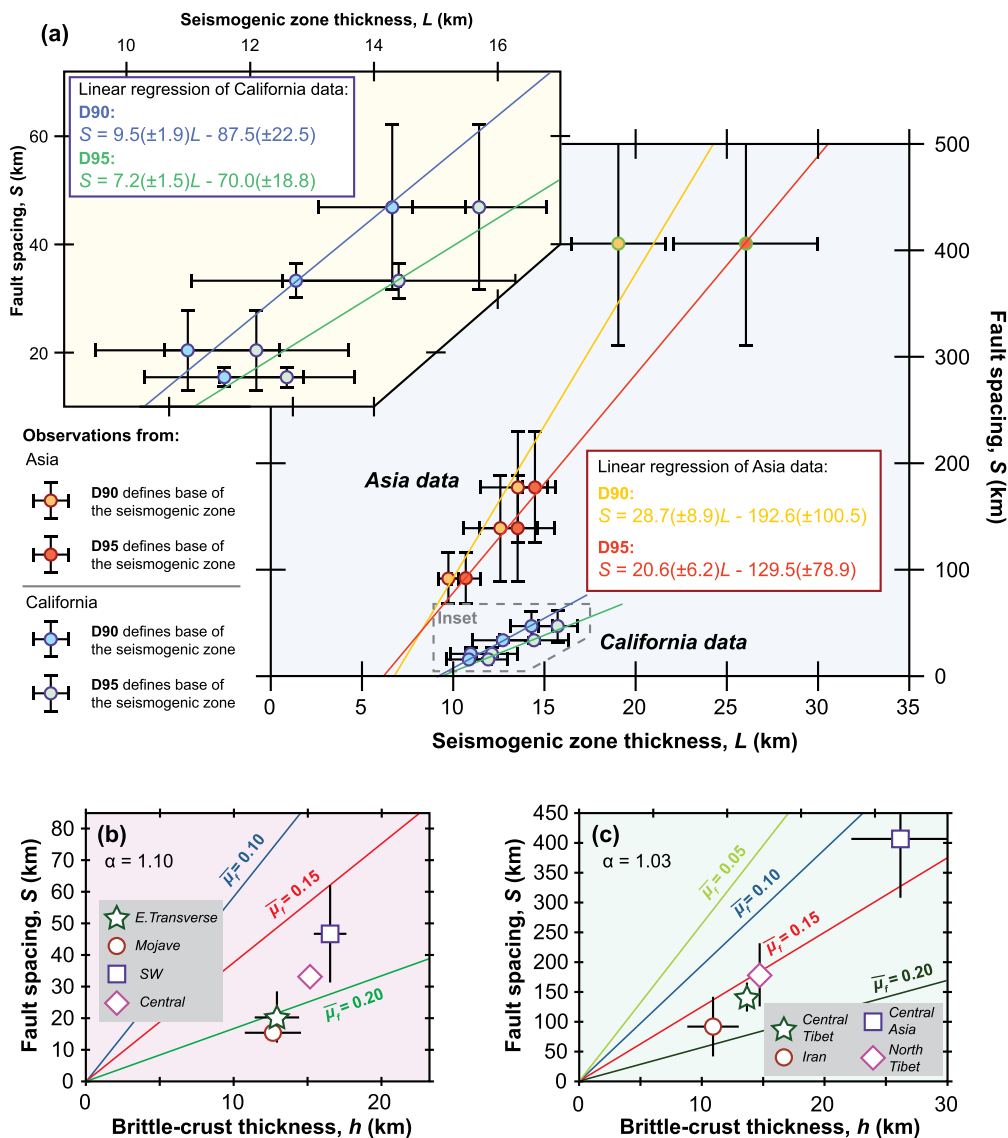
Fig. 7. (a) Plot of seismogenic zone thickness (using both D90 and D95 values) versus fault spacing for Asia and California. The inset shows an enlarged plot of the California data. The best-fit linear regressions for the seismogenic zone thickness data using either the D90 or D95 data show similar slopes. Note the negative vertical and positive horizontal intercepts for the regression lines. (b–c) Relationship between fault spacing (S) and brittle-crust thickness (h) for given α values. Plots for faults in (b) California use $\alpha = 1.10$ and (c) Asia use $\alpha = 1.03$. Other parameters used in the plots are $\overline{\mu_\varphi} = 0.24$, $\rho = 3$ g/cm^3, and $(C_0 - C_1) = 0$ MPa.

6. Discussion

Observations from our analogue experiments and crustal-scale strike-slip faults reveal a fundamental observation that fault spacing (S) is linearly proportional to brittle-layer thickness (h). Our physical models show this relationship to hold for experiments with solely frictional materials (Fig. 4d) and for two-layer experiments with a viscous layer underlying frictional materials (Fig. 4e).

6.1. Minimum and maximum thickness cutoffs for generating strike-slip faults

In our analogue experiments, strike-slip faults were only generated when the thickness of the frictional materials was between ~1 cm and ~7 cm (Fig. 4), which suggests that minimum (h_0) and maximum (h_{max}) brittle-layer cutoff thicknesses exist for generating strike-slip faults. The regressions of continental strike-slip S versus h yield negative vertical-axis intercepts for both the Asian and Californian datasets (Fig. 7a). The simplest explanation for these negative intercepts is that there is a minimum cutoff thick-

ness for nucleating continental strike-slip faults. As previously discussed (section 4.2), the boundary conditions that drive strike-slip faulting in the analogue experiments are different from those assumed in the derivation of our stress-shadow model. Thus, the brittle-layer cutoff thickness values for each setting require different explanations.

In our stress-shadow model for crustal-scale strike-slip faulting, the regional shear stress (σ_s^r) and shear fracture strength ($\overline{Y}$) increase linearly with depth (h). The two quantities also have intercepts at the surface ($h = 0$), with their values equal to C_0 and C_2 as defined in equations (7) and (9). Although we assume $C_0 = C_2$ in our stress-shadow derivation, their difference may explain the minimum cutoff value for the observed fault spacing in continental settings (Fig. 7a). Given that the regional shear stress (σ_s^r) and shear fracture strength ($\overline{Y}$) also have different slopes, these two lines must intersect in the σ_s^r and $\overline{Y}$ vs. h plot (Fig. 8a). Thus, the portion of the shear stress curve below the strength curve defines the value for the minimum fault-spacing cutoff (i.e., h_0 in Fig. 8a). Although the above explanation may apply to crustal-scale strike-slip faults, it is clearly not applicable to the occurrence of

Continental strike-slip faulting (fault-parallel shear)

Analogue experiment strike-slip faulting (basal shear)
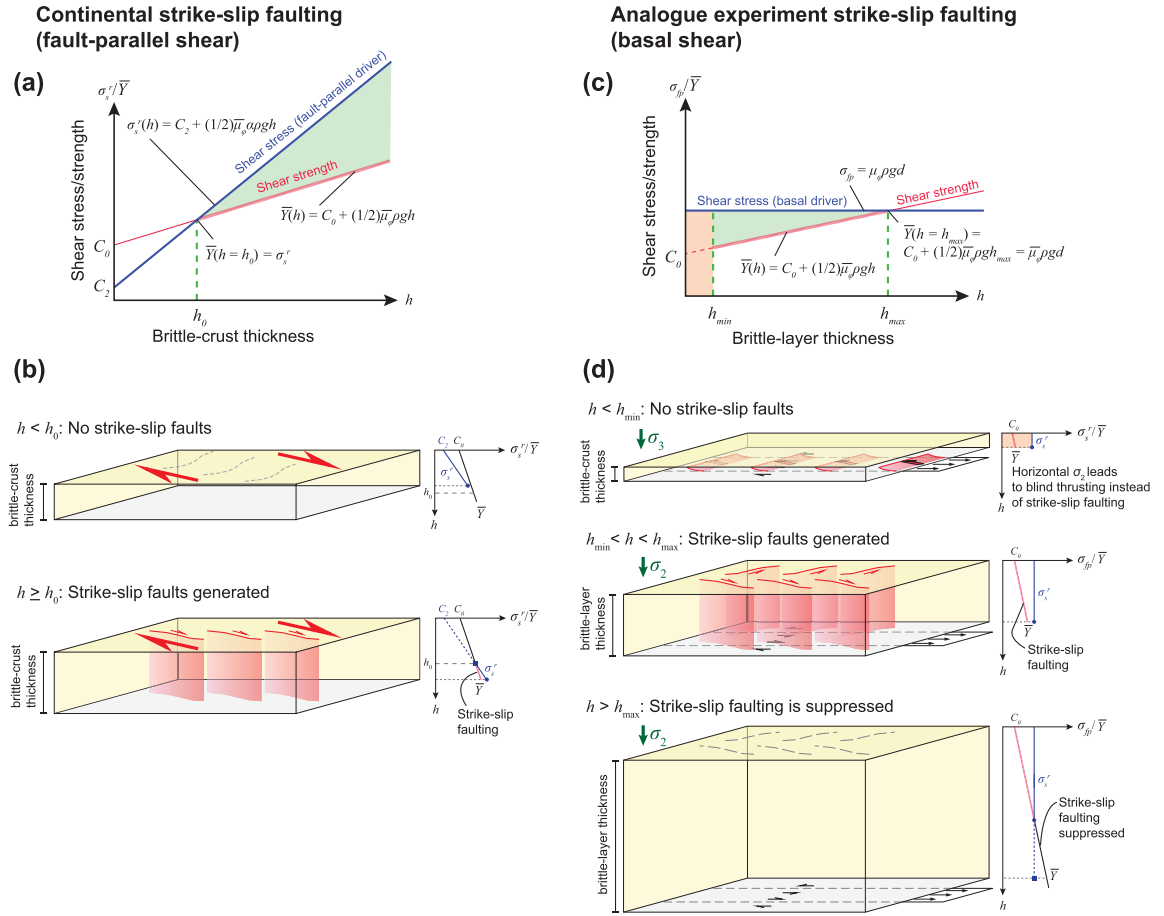
Fig. 8. (a) Conceptual plot of dimensionless shear stress/strength versus brittle-crust thickness showing the inferred minimum brittle-crust thickness (h_0) cutoff for the formation of continental strike-slip faults. Strike-slip faults will only be generated when the regional shear stress σ_s^r, which is linearly proportional to h, exceeds the vertically integrated shear-fracture strength of the material ($\overline{Y}$) at a critical brittle-curst thickness h_0. (b) Two scenarios for the continental strike-slip faulting that highlight the concepts in (a). When the brittle-crust is too thin ($h < h_0$), the regional shear stress is not large enough to surpass the vertically averaged shear-fracture strength of the crust, and no strike-slip faults are formed. When the brittle-crust thickness is greater than the cutoff thickness, strike-slip faulting can occur. (c) Conceptual plot of dimensionless shear stress/strength versus brittle-crust thickness showing the minimum (h_{min}) and maximum (h_{max}) brittle-layer thickness cutoffs for strike-slip faulting in the analogue experiments. The depth-independent fault-parallel shear stress (σ_{fp}) intersects the depth-dependent shear-fracture strength ($\overline{Y}$) curve at a critical thickness h_{max}. Above this thickness value, strike-slip faulting is suppressed by the strength of the material. Below some threshold thickness h_{min}, strike-slip faults are also not formed. (d) Three scenarios for strike-slip faulting in the analogue experiments. When h is too low, there is a switch of the principal stress directions, from σ_2 being vertical for the strike-slip regime when $h > h_{min}$ to σ_2 being horizontal for dip-slip fault regime when $h < h_{min}$, which results in blind thrusting and folding rather than strike-slip faulting. Additionally, when the brittle layer is too thick ($h > h_{max}$), the vertically averaged shear strength ($\overline{Y}$) of the brittle layer is greater than σ_{fp}, which suppresses strike-slip faulting. Strike-slip faulting does occur when $h_{min} < h < h_{max}$. Note that the green arrows indicate the principal stress orientation. (For interpretation of the references to color in this figure legend, the reader is referred to the web version of this article.)

strike-slip faults whose spacing is on the order of 10s to 100s m. These smaller scale faults are not controlled by the thickness of the brittle crust but rather local bedding thickness and/or reactivation of pre-existing fractures as commonly observed at outcrop scales (e.g., Aydin and Johnson, 1978; Segall and Pollard, 1983; Martel and Pollard, 1989).

In our analogue experiments, the effective fault-parallel shear stress (σ_{fp}) is not depth-dependent (Fig. 8c) (see section 4.2 and Supplementary Material). However, the vertically averaged shear fracture strength ($\overline{Y}$) of the sand/crushed walnut shells in our experiments does vary with h (Fig. 8c). For lower brittle-layer thickness values ($h < {\sim}7$ cm), σ_{fp} is greater than $\overline{Y}$ and parallel strike-slip faulting occurs (Fig. 8d). When h exceeds some critical thickness (i.e., h_{max} in Fig. 8c), the shear fracture strength $\overline{Y}$ surpasses the fault-parallel shear stress σ_{fp} (i.e., $\overline{Y} > \sigma_{fp}$), and Riedel-shear fracturing is suppressed (Fig. 8d).

Our experiments show that Riedel-shear fractures are not created when the brittle-layer thickness is $< {\sim}1$ cm for sand and $< {\sim}3$ cm for crushed walnut shells (Fig. 5d). The fact that this minimum thickness, h_{min}, varies for different density materials in-

dicates that the vertical stress must play a controlling role in determining the condition that favors strike-slip faulting. We tentatively suggest that the reduction of the sand/crushed walnut shell thickness leads to a switch of the principal stress directions, from σ_2 being vertical for the strike-slip regime when $h > h_{min}$ to σ_2 being horizontal for dip-slip fault regime when $h < h_{min}$. We further interpret that the inferred dip-slip faulting may be blind and concentrated immediately above the sliding-plate surface at the base of the experimental materials. Given the brittle-layer thickness uncertainties of ${\sim}1$ mm, any blind structures would have been indiscernible at the surface during the smallest thickness experiments.

The intersection of the shear fracture strength and shear stress curves in Fig. 8c can be used to further verify the stress-shadow model. At $h = h_{max}$, $\overline{Y} = \sigma_{fp}$ which requires

$$C_0 + \frac{1}{2}\mu_\varphi \rho g h_{max} = \mu_b \rho g d \times \cos 2\theta \qquad (17)$$

The maximum cutoff thickness for the sand and crushed walnut shell experiments were ${\sim}6$ cm and ${\sim}7$ cm respectively. By incorporating the frictional properties of the experimental materials

(Table 1) into equation (17), we can estimate d. For both the sand and crushed walnut shell experiments, the calculated d value is ~0.04 m. Figs. 4b and 4c show that the boundaries of Riedel shear zones are 2–4 cm from basal-sliding plate center, which corroborates this result.

6.2. Effects of a diffuse brittle-ductile transition and fault healing on brittle-crust thickness

We previously assumed that the seismogenic zone thickness directly equates to the brittle-crust thickness. The seismogenic zone (L) likely consists of both a purely frictional-sliding layer (h_f) and a transitional zone (h_{fv}) of frictional sliding and viscous creeping (Fig. 3), such that $L = h_f + h_{fv}$. This diffuse brittle-ductile transition zone should have a maximum thickness of a few kilometers. Assuming that h_{fv} is relatively constant globally, a systematic overestimation of the brittle-crust thickness ($h = h_f$) by several kilometers in both Asia and California (Fig. 7) would affect the vertical-axis intercept of the S–h linear regression but the S/h slope should remain the same.

In addition, the fault cohesive strength may be locally greater than the crustal cohesive strength (i.e., $C_1 > C_0$) due to fault healing effects (e.g., Tenthorey and Cox, 2006). Given equation (11), this condition would lead to a negative vertical-axis intercept on a S versus h plot (e.g., Fig. 7a). This seems counterintuitive but may be applicable to Asia and California where penetrative fracturing, expressed by the widespread off-fault seismicity (e.g., Chu et al., 2009; Hauksson, 2011), may have reduced the cohesive strength of the deforming crust. That is, the actively forming fractures away from through-going faults are mostly isolated, creating dead pores that are less likely to be healed by chemical precipitation than the well-connected fracture networks in active fault zones after major rupture events (Tenthorey and Cox, 2006). Thus, we may rewrite the seismogenic thickness L more completely as $L = (h' + h_{FH}) + h_{fv}$, where h' is the *effective brittle-crust thickness* and h_{FH} is the *pseudo brittle-crust thickness* induced by fault healing. Only if $h_{FH} = h_{fv} = 0$ does the seismogenic thickness L equal the brittle-crust thickness $h' = h$. Because the effects of fault healing and a diffuse brittle-crust transition counteract each other, and any healing effects must be minor because the strike-slip faults are still active, we reasonably assume that $L = h$ (Fig. 7a).

6.3. Formation of irregularly-spaced strike-slip faults

Northeast-striking right-slip faults in northern China are irregularly spaced at intervals ranging from ~100 km in the west to >500 km in the east (Yin et al., 2015). Equation (12) implies that irregularly spaced faults may be generated if the (a) strengths of the parallel faults are different, (b) fault-bounded crust has spatially varying shear strengths, and/or (c) thickness of the fault-hosting layer varies in laterally. The seismogenic thickness across North China varies from ~20 km in the west to >30 km in the east (Wang et al., 2013), which correlates with closer fault spacing in the west (Yin et al., 2015). Alternatively, spatially varying crustal strength or fault strength may locally affect faulting in northern China.

Related to such heterogeneities, the role of preexisting weaknesses in controlling fault spacing should not be underestimated. Major fault systems will inevitably exploit preexisting weaknesses (e.g., Segall and Pollard, 1983; Martel and Pollard, 1989) but an overarching fundamental mechanism controls the observed even spacing of active crustal-scale strike-slip faults (Fig. 1). Although the strike-slip faults in northern Tibet parallel Phanerozoic sutures (Zuza and Yin, 2016) and some of the strike-slip faults in California exploit preexisting normal faults (Dokka, 1989), most of the parallel strike-slip faults discussed here crosscut the regional structural trend (Fig. 1).

6.4. Role of the lower crust driving strike-slip faulting

Regional shear stress σ^{bc} (or σ_s^r) is a key parameter that drives faulting in the stress-shadow model (Fig. 3). In our derivation for continental strike-slip faults we assumed that σ_s^r equals $\overline{Y^{BR}}$ (Fig. 3). Alternatively, distributed basal shear in a viscous lower crust may drive or influence the regional shear stress σ_s^r acting on the brittle crust (e.g., Roy and Royden, 2000a, 2000b). Our sand–putty analogue experiments demonstrate how the rheological and/or geometric properties of the underlying viscous layer may affect brittle-layer fault spacing.

Interpretation of the two-layer brittle–viscous experiments is not as straightforward as the single-brittle-layer experiments. In section 4.2 we showed that although the boundary conditions for our experimental setup are different from our theoretical model (e.g., Fig. 3 vs. Fig. 4), the derived fault-parallel shear stress in our experiments, σ_{fp}, is equivalent to the regional shear stress, σ^{bc}, of Fig. 3. The single-layer brittle-material experiments involved rate-independent frictional materials and a constant basal-sliding-plate velocity throughout all trials. This allows for investigation of the brittle-layer thickness versus fault spacing relationship (i.e., the S/h correlation in Fig. 4d) and for direct comparison of the experiments and our theoretical model, without including extra variables such as loading rate (i.e., basal-sliding-plate velocity). However, the brittle–viscous experiments involved a rate-dependent viscous-putty-layer with variable thicknesses and viscosities (Fig. 4e). Although all trials used a constant basal-sliding-plate velocity, the thickness and viscosity variations of the putty layer in these trials inversely and directly affected, respectively, the basal stress acting on the overlying frictional-sand layer. Thus, even with a constant basal-sliding-plate velocity, the basal loading rate acting on the sand layer varied for experiments with different putty thicknesses and viscosities, and therefore direct quantitative comparison between the putty-layer experiments is not possible. In viewing Fig. 4e, we emphasize that the three sets of trials with similar viscosities and putty thicknesses involve minor differences in different basal loading rates. Even though the time-dependent viscous layer complicates our analysis, the linear S/h relationship for each set of trials with similar initial conditions (e.g., putty thickness or viscosity) gives us some confidence that our results provide meaningful qualitative insight into how an underlying viscous layer affects deformational processes in the overlying frictional layer.

The viscous putty may affect the S/h slope in the overlying brittle layer in several ways: (1) the viscosity and/or thickness of the putty controls the basal shear stress acting on the brittle materials, (2) distributed basal loading causes a variable-width basal shear zone, and/or (3) the frictional interaction at the sand-putty interface affects the basal-shear stress acting on the overlying brittle materials (i.e., coupling between the viscous and brittle layers). As described below, these first two scenarios do not appear to dominantly control fault spacing in the overlying brittle layer.

The viscosity and thickness parameters of the viscous putty should be proportional and inversely proportional to the maximum basal shear stress driven by motion within the underlying viscous material, respectively. Experiments with thicker and/or lower viscosity putty will have a lower possible basal shear stress, whereas thinner and/or higher viscosity putty layer should generate a higher basal shear stress. Fig. 4e shows the results of our trials using putty layers with different viscosities and thicknesses. If these viscous-layer properties directly affect brittle-layer fault spacing, then the observed S/h slope should vary systematically according to our stress-shadow model. That is, thicker and/or lower viscosity putty trials (i.e., lower basal shear stress) should

have a steeper S/h relationship, whereas thinner and/or higher viscosity putty experiments (i.e., higher basal shear stress) should result in a shallower S/h slope (e.g., Figs. 3 and 5). Our experiments do not show these systematic variations (Fig. 4e). The thicker/less viscous putty experiments yield the shallowest S/h slopes (i.e., blue squares in Fig. 4e). Conversely, the thinner and/or more viscous putty experiments yield steeper S/h slopes (i.e., green and red symbols in Fig. 4e).

Based on our understanding of the stress-shadow mechanism as it relates fault spacing to basal stress (see section 4.2 and Supplementary Material), fault-parallel shear stress (σ_{fp}) is a function of d and μ_b as in equation (16). If distributed basal loading across a ductile shear zone affects brittle-layer fault spacing, we would expect that the viscous-layer experiments would involve relatively distributed basal shear when compared to the granular material-only trials. This would lead to a decreased d value in equation (16) and thus an increased S/h slope, which is not observed (Fig. 4e).

The coefficient of friction between the sand and putty (i.e., μ_b of equation (16)) is 0.73, which is higher than for sand against sand paper (Table 1). The higher μ_b for the sand–putty experiments should lead to a reduced S/h slope, which is observed in the sand–putty experiments (Fig. 4e). Furthermore, all else being equal, equation (16) predicts that given the measured μ_b values for each set of experiments (Table 1), the sand-only experiments will have a S/h slope that is ~1.3 times that of the sand–putty experiments. This slope difference is observed: the 0.68 S/h slope for the sand-only experiments is ~1.2–1.3 times the ~0.52 slope for the sand–putty experiments (Figs. 4d and 4e). These results suggest that the friction coefficient at viscous–brittle layer interface (i.e., the coupling between the two layers) affects the strike-slip fault spacing in the brittle layer more than the effects of the distributed basal shear by the viscous layer or the rheological variations of this viscous layer. These findings contrast the viscoelastic models of Roy and Royden (2000a, 2000b).

Although we present a linear stress-shadow model, our general solution can be modified for other values of m and n. For example, the addition of a viscous layer may make our assumed simple linear relationship more complex, and future work is needed to explore other possible nonlinear solutions that may ultimately be useful for understanding the shear-stress distribution in two-layer viscous–brittle systems. However, we assert that the observed linear relationship between fault spacing and brittle-layer thickness in both our analogue experiments and crustal-scale strike-slip faults validates our application of a linear stress-shadow model to continental strike-slip faults.

6.5. Estimates of absolute fault friction from fault spacing and seismogenic zone thickness

The observed difference in S/h slope between Asia and California must reflect differences in how the faults interact with one another and with the fault-bounded crust. Based on equation (12) and assuming that the crustal internal coefficient of friction $\overline{\mu_\varphi}$ for both continents is the same, the steep S/h slope observed in Asia may result from a lower magnitude of effective fault friction ($\overline{\mu_f}$), a higher magnitude regional shear stress, or a combination of factors.

In California, the seismogenic thicknesses of the relatively stable Western Transverse and Central Valley–Sierra regions were compared with the L values of the adjacent deforming regions (Fig. 6) to estimates $\alpha = H/h$ values of 1.05 to 1.2. Using regionally averaged $\alpha = 1.1$ and $\overline{\mu_\varphi} = 0.24$ values, we find that the closely spaced faults in the eastern San Andreas fault system are stronger at $\overline{\mu_f} = 0.18$–0.22 than the widely spaced faults in the western San Andreas fault system at $\overline{\mu_f} = 0.15$–0.18 (Fig. 7b). Because of the sparser data in Asia, we are unable to resolve between the internal variation of seismogenic zone thickness in a single strike-slip domain (h) and its difference from the seismogenic zone thickness of its bounding regions (H). We take this to indicate $\alpha = H/h \approx 1.0$. Available earthquake data near the edges of the central Asia strike-slip domain yield an α value of ~1.03. Using this value for all the strike-slip systems in Asia, we find their strength to be weaker ($\overline{\mu_f} =\sim 0.10$–0.20) than the fault strength in the San Andreas system ($\overline{\mu_f} =\sim 0.15$–0.22) (Figs. 7b and 7c). The weak faults in Asia and relatively stronger faults in California are consistent with existing fault-strength studies (e.g., Bird and Kong, 1994; Vernant and Chéry, 2006; Fay and Humphreys, 2006; Humphreys and Coblentz, 2007; He and Chéry, 2008). Note that if our assumption of $n = m = 1$ in equation (4) is incorrect, and these values both equal 2 (i.e., similar to the LEFM stress-distribution solution), then the corresponding $\overline{\mu_f}$ estimates for faults in both California and Asia would decrease; all would be <0.10.

The San Andreas transform fault boundary and Asia both experience large strike-slip earthquakes (Figs. 1a and 1b). The relatively weak faults in Asia (Fig. 7c) may explain the long-puzzling observation that active deformation induced by the indentation of India extends ~3500 km north of the Himalaya (Fig. 1b). Specifically, the weakest faults in Asia (i.e., in Central Asia and northern Tibet) (Fig. 7c) are also the farthest from the India–Asia collisional front, which permits intra-continental deformation to occur within the Asian interior. The slippery faults in Asia make them sensitive to minor changes in crustal stress magnitude, which explains why the Asian interior is prone to large ($M > 7.0$) devastating strike-slip earthquakes (Fig. 1b). The weaker faults in both locations can be readily explained by their hosting crustal compositions containing friction-reducing clays and hydrated phyllosilicates (e.g., Collettini et al., 2009): central Asia is dominated by flysch complexes (e.g., Sengör et al., 1993) and the western San Andreas system is dominated by mélange and forearc materials (e.g., Dickinson, 1981). Constraining fault strength is critical in modeling continental deformation (Bird and Kong, 1994) and earthquake mechanics (Console et al., 2015), and this work provides an additional method of estimating this critical parameter.

7. Conclusions

In this study we have shown that strike-slip fault spacing is linearly proportional to brittle-layer thickness in nature and scaled analogue experiments. Specifically, this relationship can be quantified as a function of brittle-crust thickness, fault strength, and regional stress state with our newly developed stress-shadow model. The application of this model using seismogenic zone thickness and fault spacing reveals that the closely spaced faults in the eastern San Andreas system are stronger than the widely spaced faults in the western San Andreas system. Furthermore, we find that the average friction coefficient of active strike-slip faults in the India–Asia collision orogen is lower than that of faults in the San Andreas transform system.

Appendix A. Supplementary material

Supplementary material related to this article can be found online at http://dx.doi.org/10.1016/j.epsl.2016.09.041.

References

Aydin, A., Johnson, A.M., 1978. Development of faults as zones of deformation bands and as slip surfaces in sandstone. Pure Appl. Geophys. 116, 931–942.

Bachmanov, D.M., Trifonov, V.G., Hessami, K.T., Kozhurin, A.I., Ivanova, T.P., Rogozhin, E.A., Hademi, F.H., Jamali, F.H., 2004. Active faults in the Zagros and central Iran. Tectonophysics 380 (3), 221–241.

Bai, T., Pollard, D.D., 2000. Fracture spacing in layered rocks: a new explanation based on the stress transition. J. Struct. Geol. 22 (1), 43–57.

Bird, P., Kong, X., 1994. Computer simulations of California tectonics confirm very low strength of major faults. Geol. Soc. Am. Bull. 106 (2), 159–174.

Burtman, V.S., Molnar, P., 1993. Geological and geophysical evidence for deep subduction of continental crust beneath the Pamir. Spec. Publ., Geol. Soc. Am. 291, 1–76.

Chu, R., Zhu, L., Helmberger, D.V., 2009. Determination of earthquake focal depths and source time functions in central Asia using teleseismic P waveforms. Geophys. Res. Lett. 36 (17).

Collettini, C., Niemeijer, A., Viti, C., Marone, C., 2009. Fault zone fabric and fault weakness. Nature 462 (7275), 907–910.

Console, R., Carluccio, R., Papadimitriou, E., Karakostas, V., 2015. Synthetic earthquake catalogs simulating seismic activity in the Corinth Gulf, Greece, fault system. J. Geophys. Res., Solid Earth 120 (1), 326–343.

Cruz, L., Teyssier, C., Perg, L., Take, A., Fayon, A., 2008. Deformation, exhumation, and topography of experimental doubly-vergent orogenic wedges subjected to asymmetric erosion. J. Struct. Geol. 30 (1), 98–115.

Davy, P., Cobbold, P.R., 1988. Indentation tectonics in nature and experiment. 1. Experiments scaled for gravity. Bull. Geol. Inst. Univ. Upps. 14, 129–141.

Dickinson, W.R., 1981. Plate tectonic evolution of the southern Cordillera. Relations of tectonics to ore deposits in the southern Cordillera. Ariz. Geol. Soc. Dig. 14, 113–135.

Dickinson, W.R., 1996. Kinematics of transrotational tectonism in the California Transverse Ranges and its contribution to cumulative slip along the San Andreas transform fault system. Spec. Pap., Geol. Soc. Am. 305, 1–46.

Dokka, R.K., 1989. The Mojave extensional belt of southern California. Tectonics 8 (2), 363–390.

Dokka, R.K., Travis, C.J., 1990. Late Cenozoic strike-slip faulting in the Mojave desert, California. Tectonics 9, 311–340.

Fay, N., Humphreys, E., 2006. Dynamics of the Salton block: absolute fault strength and crust–mantle coupling in Southern California. Geology 34 (4), 261–264.

Fossen, H., Schultz, R.A., Shipton, Z.K., Mair, K., 2007. Deformation bands in sandstone: a review. J. Geol. Soc. 164 (4), 755–769.

Freund, R., 1974. Kinematics of transform and transcurrent faults. Tectonophysics 21 (1), 93–134.

Gross, M.R., 1993. The origin and spacing of cross joints: examples from the Monterey Formation, Santa Barbara Coastline, California. J. Struct. Geol. 15 (6), 737–751.

Hauksson, E., 2011. Crustal geophysics and seismicity in southern California. Geophys. J. Int. 186 (1), 82–98.

Hauksson, E., Yang, W., Shearer, P.M., 2012. Waveform relocated earthquake catalog for southern California (1981 to June 2011). Bull. Seismol. Soc. Am. 102 (5), 2239–2244.

He, J., Chéry, J., 2008. Slip rates of the Altyn Tagh, Kunlun and Karakorum faults (Tibet) from 3D mechanical modeling. Earth Planet. Sci. Lett. 274 (1), 50–58.

Hubbert, M.K., 1937. Theory of scale models as applied to the study of geologic structures. Geol. Soc. Am. Bull. 48 (10), 1459–1520.

Hubbert, M.K., 1951. Mechanical basis for certain familiar geologic structures. Geol. Soc. Am. Bull. 62 (4), 355–372.

Humphreys, E.D., Coblentz, D.D., 2007. North American dynamics and western US tectonics. Rev. Geophys. 45 (3).

Jackson, J., McKenzie, D., Priestley, K., Emmerson, B., 2008. New views on the structure and rheology of the lithosphere. J. Geol. Soc. 165 (2), 453–465.

Jaeger, J.C., Cook, N.G., Zimmerman, R., 2009. Fundamentals of Rock Mechanics. John Wiley & Sons.

Lachenbruch, A.H., 1961. Depth and spacing of tension cracks. J. Geophys. Res. 66 (12), 4273–4292.

Lin, G., Shearer, P.M., Hauksson, E., 2007. Applying a three-dimensional velocity model, waveform cross correlation, and cluster analysis to locate southern California seismicity from 1981 to 2005. J. Geophys. Res., Solid Earth 112 (B12).

Lister, G.S., Davis, G.A., 1989. The origin of metamorphic core complexes and detachment faults formed during Tertiary continental extension in the northern Colorado River region, U.S.A. J. Struct. Geol. 11 (1), 65–94.

Maggi, A., Jackson, J.A., Priestley, K., Baker, C.A., 2000. A reassessment of focal depth distributions in southern Iran, the Tien Shan and northern India: do earthquakes really occur in the continental mantle? Geophys. J. Int. 143, 629–661.

Martel, S.J., Pollard, D.D., 1989. Mechanics of slip and fracture along small faults and simple strike-slip fault zones in granitic rock. J. Geophys. Res., Solid Earth 94 (B7), 9417–9428.

Molnar, P., Tapponnier, P., 1975. Cenozoic tectonics of Asia: effects of a continental collision. Science 189 (4201), 419–426.

Naylor, M.A., Mandl, G.T., Supesteijn, C.H.K., 1986. Fault geometries in basement-induced wrench faulting under different initial stress states. J. Struct. Geol. 8 (7), 737–752.

Nur, A., Ron, H., Scotti, O., 1986. Fault mechanics and the kinematics of block rotations. Geology 14 (9), 746–749.

Pollard, D.D., Segall, P., 1987. Theoretical displacements and stresses near fractures in rock: with applications to faults, joints, veins, dikes, and solution surfaces. Fract. Mech. Rock 277 (349), 277–349.

Roy, M., Royden, L.H., 2000a. Crustal rheology and faulting at strike-slip plate boundaries: 1. An analytic model. J. Geophys. Res., Solid Earth 105 (B3), 5583–5597.

Roy, M., Royden, L.H., 2000b. Crustal rheology and faulting at strike-slip plate boundaries: 2. Effects of lower crustal flow. J. Geophys. Res., Solid Earth 105 (B3), 5599–5613.

Savage, J.C., Lisowski, M., 1993. Inferred depth of creep on the Hayward fault, central California. J. Geophys. Res., Solid Earth 98 (B1), 787–793.

Schaff, D.P., Waldhauser, F., 2005. Waveform cross-correlation-based differential travel-time measurements at the Northern California Seismic Network. Bull. Seismol. Soc. Am. 95 (6), 2446–2461.

Segall, P., Pollard, D.D., 1983. Nucleation and growth of strike slip faults in granite. J. Geophys. Res., Solid Earth 88 (B1), 555–568.

Sengör, A.M.C., Natal'In, B.A., Burtman, V.S., 1993. Evolution of the Altaid tectonic collage and Palaeozoic crustal growth in Eurasia. Nature 364, 299–307.

Sloan, R.A., Jackson, J.A., McKenzie, D., Priestley, K., 2011. Earthquake depth distributions in central Asia, and their relations with lithosphere thickness, shortening and extension. Geophys. J. Int. 185 (1), 1–29.

Swanson, M.T., 1988. Pseudotachylyte-bearing strike-slip duplex structures in the Fort Foster Brittle Zone, S. Maine. J. Struct. Geol. 10 (8), 813–828.

Taylor, M., Yin, A., 2009. Active structures of the Himalayan–Tibetan orogen and their relationships to earthquake distribution, contemporary strain field, and Cenozoic volcanism. Geosphere 5 (3), 199–214.

Tchalenko, J.S., 1970. Similarities between shear zones of different magnitudes. Geol. Soc. Am. Bull. 81 (6), 1625–1640.

Tenthorey, E., Cox, S.F., 2006. Cohesive strengthening of fault zones during the interseismic period: an experimental study. J. Geophys. Res., Solid Earth 111 (B9).

Vernant, P., Chéry, J., 2006. Low fault friction in Iran implies localized deformation for the Arabia–Eurasia collision zone. Earth Planet. Sci. Lett. 246 (3), 197–206.

Waldhauser, F., Schaff, D.P., 2008. Large-scale relocation of two decades of Northern California seismicity using cross-correlation and double-difference methods. J. Geophys. Res., Solid Earth 113 (B8).

Wang, J., Dapeng, Z., Yao, Z., 2013. Crustal and uppermost mantle structure and seismotectonics of North China Craton. Tectonophysics 582, 177–187.

Yin, A., 2010. Cenozoic tectonic evolution of Asia: a preliminary synthesis. Tectonophysics 488 (1), 293–325.

Yin, A., Taylor, M.H., 2011. Mechanics of V-shaped conjugate strike-slip faults and the corresponding continuum mode of continental deformation. Geol. Soc. Am. Bull. 123 (9–10), 1798–1821.

Yin, A., Yu, X., Shen, Z.K., Liu-Zeng, J., 2015. A possible seismic gap and high earthquake hazard in the North China Basin. Geology 43 (1), 19–22.

Yin, A., Zuza, A.V., Pappalardo, R.T., 2016. Mechanics of evenly spaced strike-slip faults and its implications for the formation of tiger-stripe fractures on Saturn's moon Enceladus. Icarus 266, 204–216.

Zuza, A.V., Yin, A., 2016. Continental deformation accommodated by non-rigid passive bookshelf faulting: an example from the Cenozoic tectonic development of northern Tibet. Tectonophysics 677, 227–240.